




Article

Structure and Molecular Dynamics in Metal-Containing Polyamide 6 Microparticles

Filipa M. Oliveira ^{1,†} , Teresa G. Nunes ², Nadya V. Dencheva ¹  and Zlatan Z. Denchev ^{1,*} 

¹ Institute for Polymers and Composites, Department of Polymer Engineering, University of Minho, 4800-058 Guimarães, Portugal

² Centro de Química Estrutural, Instituto Superior Técnico, Universidade de Lisboa, Av. Rovisco Pais, 1049-001 Lisboa, Portugal

* Correspondence: denchev@dep.uminho.pt

† Current Address: Department of Inorganic Chemistry, University of Chemistry and Technology Prague, Technická 5, 16628 Prague 6, Czech Republic.

Abstract: Polymer microparticles are used in additive manufacturing, separation and purification devices, biocatalysis, or for the recognition of biomolecules. This study reports on the effect of metal fillers on the structure and molecular dynamics of polyamide 6 (PA6) microparticles (MPs) containing up to 19 wt.% of Al, Cu, or Mg. These hybrid MPs are synthesized via reactive microencapsulation by anionic ring-opening polymerization in solution, in the presence of the metal filler. ¹³C high-resolution solid-state NMR (ssNMR) spectroscopy is employed as the primary characterization method using magic angle spinning (MAS) and cross-polarization (CP)/MAS. Depending on the metal filler, the ssNMR crystallinity index of the MP varies between 39–50%, as determined by deconvolution of the ¹³C MAS and CP/MAS spectra. These values correlate very well with the crystallinity derived from thermal or X-ray diffraction data. The molecular dynamics study on PA6 and Cu-containing MP shows similar mobility of carbon nuclei in the kHz, but not in the MHz frequency ranges. The paramagnetic Al and Mg have an observable effect on the relaxation; however, conclusions regarding the PA6 carbon motions cannot be unequivocally made. These results are useful in the preparation of hybrid microparticles with customized structures and magneto-electrical properties.

Keywords: polymer microparticles; metal particles; ¹³C solid-state NMR; crystalline structure; relaxation times



Citation: Oliveira, F.M.; Nunes, T.G.; Dencheva, N.V.; Denchev, Z.Z. Structure and Molecular Dynamics in Metal-Containing Polyamide 6 Microparticles. *Crystals* **2022**, *12*, 1579. <https://doi.org/10.3390/cryst12111579>

Academic Editor: Eamor M. Woo

Received: 23 September 2022

Accepted: 2 November 2022

Published: 5 November 2022

Publisher's Note: MDPI stays neutral with regard to jurisdictional claims in published maps and institutional affiliations.



Copyright: © 2022 by the authors. Licensee MDPI, Basel, Switzerland. This article is an open access article distributed under the terms and conditions of the Creative Commons Attribution (CC BY) license (<https://creativecommons.org/licenses/by/4.0/>).

1. Introduction

Polyamides are semicrystalline polymers, which are widely used as engineering thermoplastics in numerous applications due to their unique combination of mechanical, thermal, and chemical resistance [1]. The advent of layer-by-layer additive manufacturing technologies, such as selective laser sintering (SLS), has provided a powerful impetus for the in-depth characterization of polyamide micron-sized particles. It is now known beyond any doubt that the correct choice of powder material containing particles with suitable size, shape, rheology, melting, and crystallization behavior is fundamental for the successful SLS to final articles with optimized mechanical properties [2,3].

Most frequently, *neat* polyamide microparticles (MP) appropriate for SLS are prepared by physical methods, including dissolution-precipitation [4], melt emulsification [5], or cryogenic milling [6]. Alternatively, a recently developed chemical approach based on solution-precipitation activated anionic ring-opening polymerization (AAROP) of lactams [7,8] allowed for the preparation of *hybrid* polyamide MP systems with polyamide 6 (PA6) shells, which can carry elevated amounts of metal, ceramic, or carbon allotropes, as well as mixed payloads. Among these hybrid particulate systems, the metal-loaded PA6 MP can be especially interesting for the development of novel lightweight materials with

tailored magnetic susceptibility, electric and thermal conductivity, or electromagnetic interference (EMI) shielding properties [9,10]. Recent reports on a PA6-based metal-containing hybrid MP showed that they can be used directly as supports for enzymes in biosensors and biocatalysts [11,12], or be transformed by melt processing into PA6-based composites with particulate or textile reinforcement [8,13].

All of these existing and potential applications of metal-containing PA6 microparticles require rigorous control over their crystalline structure and, especially in the case of EMI shielding, over the local motions in the solid-state, concerning both crystalline and amorphous phases. For this reason, the use of high-resolution solid-state NMR (ssNMR) that studies finely pulverized samples has become a powerful technique for structure properties investigation in polyamide-based particulate materials [14]. The first comprehensive structural studies by ssNMR on neat PA6 were reported in the 1980s and 1990s using carbon-13 (^{13}C) [15–18] or nitrogen-15 (^{15}N) [19–21] nuclei. Some of us have also used ^{13}C -ssNMR, along with other analytical methods, to relate the crystalline structure to the mechanical properties in neat PA6 [22] and PA12 [23]. There exist numerous ssNMR studies on the structure of PA6-based composites, mostly comprising nanosized clays [24].

To the best of our knowledge, no ssNMR studies on metal-loaded PA6 hybrids have been performed so far. Regarding other polymer matrices, only a few communications exist at this point. Thus, Umek et al. [25] prepared polystyrene nanocomposites using titanate nanostructures and analyzed their homogeneity and local chain mobility by ^1H NMR. The skin effect in high-density polyethylene loaded with Ag nanoparticles and carbon nanotubes was studied by Jouni et al., by means of ^{13}C NMR measurements [26]. It should be noted that the conventional preparation of polymer hybrids by melt processing applied in these two works requires several blending and grinding steps in order to produce the fine and homogeneous powders necessary for the ssNMR measurement.

The present work is the first ssNMR study on the structure and molecular dynamics of PA6-based metal-loaded microparticles (Me-MPs) obtained by one-pot AAROP in solution containing Al, Cu, or Mg fillers. As shown previously [27], this chemical method provides excellent distribution of the metal payloads within the PA6 particles. Importantly, the as-prepared Me-MPs are subjected directly to ssNMR without any processing, which allows the analysis of their nascent structure. Thus, the ^{13}C resonances of the semicrystalline MP samples were recorded by conventional magic angle spinning (MAS) or cross-polarization (CP)/MAS pulse sequences. Then, by deconvolution of these spectral data, the NMR degree of crystallinity in all MP samples was calculated as a function of the metal filler type. Comparisons with crystallinity data for the same MP samples obtained by differential scanning calorimetry (DSC) and synchrotron X-ray diffraction (XRD) were made and discussed. Molecular dynamics studies were performed using the ssNMR capacity to probe the molecular mobility in either amorphous or crystalline regions of MPs. The spin–lattice relaxation time in the rotating frame, $T_{1\rho}$, characterized by slower motions, and the spin–lattice relaxation time, T_1 , sensitive to rapid molecular motions, were measured [28,29]. All ssNMR, DSC, and XRD data were related to the structure of the amorphous and crystalline phases in the PA6 MP samples, and their morphology was revealed by scanning electron microscopy (SEM).

2. Materials and Methods

2.1. Chemicals and Materials

A special grade of ECL monomer with reduced moisture content was delivered by Brüggemann Chemical (Germany); C20 commercial activator of AAROP containing 80 wt.% of aliphatic diisocyanate blocked in ECL from Brüggemann Chemical (Germany); sodium dicaprolactamato-bis-(2-methoxyethoxy)-aluminate (Dilactamate, DL) AAROP initiator from Katchem (Czech Republic); metal powders from Sigma-Aldrich, Portugal: Cu (>99.5%, grain size < 40 μm); and Al (>93%, grain size < 100 μm), Mg (>99%, grain size < 100 μm), toluene, methanol, and other solvents (analytical grade) from Merck/Sigma Aldrich, Algés, Portugal.

2.2. Synthesis of Metal-Loaded PA6 MP

Metal-loaded PA6 MPs were produced by AAROP of ECL in solution, performed as described previously [7,8]. In summary: 0.5 mol of ECL and 10 wt.% of selected metal powder in relation to ECL were added to 100 mL of 1:1 toluene/xylene mixture. This was performed while stirring in a three-neck round bottom flask supplied with a Dean–Stark attachment and an Allihn condenser, under a nitrogen atmosphere, refluxing the reaction mixture for 10–15 min. Then, 3 mol.% of DL and 1.5 mol.% of C20 were added at once. The polymerization reaction was carried out for 2 h from the point of catalytic system addition, in the temperature range of 130–135 °C and at a constant stirring rate of ca. 800 rpm. The empty and the metal-containing MP samples were separated from the reaction mixture by vacuum filtration, then washed with methanol and dried for 4 h at 80 °C in a vacuum oven.

2.3. Characterization by SEM

The SEM studies were performed in a NanoSEM-200 apparatus of FEI Nova (USA) using mixed secondary electron/back-scattered electron in-lens detection. The MP samples were observed directly after sputter coating with an Au/Pd alloy in a 208 HR equipment of Cressington Scientific Instruments (UK) with high-resolution thickness control.

2.4. Characterization by ssNMR

A Tecmag Redstone/Bruker 300WB spectrometer was used. Metal-loaded MP samples (about 200 mg) were packed into 7 mm o.d. zirconia rotors with Kel-F caps. The experiments were carried out at room temperature (23 ± 0.5 °C). ^{13}C spectra were acquired at 75.49 MHz, with a spinning rate of about 3 kHz and 90° radio-frequency (RF) pulses of (i) 4 μs or (ii) 4.5 μs , using two different RF sequences: (i) one pulse (direct-excitation, Bloch decay) with 1s relaxation delay, and (ii) cross-polarization/MAS (CP/MAS) spectra with a relaxation delay of 10 s, a contact time of 2 ms, and a frequency field of 62.5 kHz for the spin-lock field B_1 . Experiments (i) and (ii) were expected to enhance amorphous and crystalline polymer components, respectively. The ^{13}C chemical shifts were obtained using the ^{13}CO glycine signal as an external reference, which was set at 176.03 ppm.

The ssNMR degree of crystallinity, X_c^{ssNMR} , of all samples was determined from the ^{13}C MAS and CP/MAS spectral data. Gaussian functions were chosen to deconvolute the C signals using the PeakFit© software. For each MP sample, the contributions of the crystalline and amorphous phases were calculated based on the areas of the peaks assigned to the respective aliphatic groups, i.e., using the signals of C nuclei with the same multiplicity, according to Equation (1):

$$X_c^{ssNMR\,partial} = \frac{\Sigma A_c}{\Sigma A_c + \Sigma A_a}, \% \quad (1)$$

where A_c is the sum of the areas of the crystalline phase signals and A_a is the sum of the areas of the amorphous phase signals for each group of aliphatic carbons. Applying equation 1 to the empty and Me-MPs, the partial X_c^{ssNMR} was calculated considering the two groups of nuclei, (C4, C2 + C3) and (C5, C1). Then, the $X_c^{ssNMR\,total}$ was determined based on the total sum of the area of all aliphatic C peaks from the crystalline phase:

$$X_c^{ssNMR\,total} = \Sigma A(C4, C2 + C3)_c + \Sigma A(C5, C1)_c, \% \quad (2)$$

The influence of metal payloads on the molecular dynamics of the polymer matrix was assessed by measuring different relaxation times which enable probing mobility at different frequencies. The carbon spin–lattice relaxation time, $^C T_1$, and the carbon spin–lattice relaxation time in the rotating frame, $^C T_{1\rho}$, were measured using ^{13}C CP/MAS experiments. $^C T_1$ was obtained in the MHz range by recording the intensity of the carbon signals as a function of the variable time delay, τ , using the TORCHIA sequence [30]. Either 14 values (from 0.5 s up to 40 s) or 10 values (from 0.5 s up to 25 s) were selected, depending on the sample type (neat PA6 MP or Me-MP, respectively). The number of scans was always higher than 120. The magnetization recorded from each C species was plotted against τ .

${}^C T_{1\rho}$ data were measured in the kHz range by recording the ${}^{13}\text{C}$ signal as a function of the ${}^{13}\text{C}$ spin-locking time t , immediately after a CP period of 2 ms; t was selected between 0.5 s and 25 s. The frequency field of the spin-locking field B_1 was kept at 62.5 kHz, and the recycle delay was 5 s.

${}^C T_1$ data were obtained using Equation (3) or (4) (mono- or double-exponential decays, respectively), and the ${}^C T_{1\rho}$ values were the time constants from mono-exponential decays (similar to Equation (3)):

$$y = I_0 \exp\left(-\frac{\tau}{({}^C T_1)_1}\right) \quad (3)$$

$$y = I_0 + I_1 \exp\left(-\frac{\tau}{({}^C T_1)_1}\right) + I_2 \exp\left(-\frac{\tau}{({}^C T_1)_2}\right) \quad (4)$$

Equation (3) or (4) were fitted to the experimental data (signal intensity as a function of τ), using the least-squares method. In all the experiments, empty PA6 MPs were studied as a reference.

2.5. Characterization by DSC

Differential scanning calorimetry (DSC) measurements were carried out in a 200 F3 equipment of Netzsch (Selb, Germany) at a heating rate of 10 °C/min under a nitrogen purge. The typical sample weights were in the 10–15 mg range. The degree of crystallinity, X_c^{DSC} , of all PA6 MPs synthesized was calculated according to Equation (5):

$$X_c^{DSC} = \frac{\Delta H_m^i}{w \cdot \Delta H_m^0}, \% \quad (5)$$

where ΔH_m^i is the registered melting enthalpy of the current sample, w is the weight fraction of the polymer present in the sample, and ΔH_m^0 is the melting enthalpy of a 100% crystalline PA6 (190 J/g) [31].

2.6. Characterization by XRD

Synchrotron wide-angle X-ray scattering measurements were performed in the NCD-SWEET beamline of the ALBA synchrotron facility in Barcelona, Spain. Two-dimensional detectors were used, namely LH255-HS (Rayonix, Evanston, IL, USA) and Pilatus 1M (Dectris, Switzerland), for registering the WAXS and SAXS patterns, respectively. The sample-to-detector distance was set to 150.3 mm for WAXS and 2696.5 mm for SAXS measurements, the λ of the incident beam was 0.1 nm, and the beam size was 0.35×0.38 mm ($h \cdot v$). The two-dimensional images from the two detectors were reduced to linear patterns using pyFAI software [32]. The X-ray crystallinity index was calculated using the commercial package Peakfit 4.12 by SeaSolve, as explained in the Supporting Information (SI).

3. Results and Discussion

3.1. Sample Synthesis, Designation and Morphology

The chemical structures of the ϵ -caprolactam (ECL) monomer, AAROP initiator, and activator, as well as a scheme of the polymerization process, are presented in Figure S1 of the Supplementary Materials (SM). The mechanism of AAROP in the solution of ECL to neat PA6 MPs was discussed in detail previously, [33] and was more recently adapted for the case of hybrid PA6 MPs including metals [7,8,27]. The metal payloads in this study were used without any pretreatment or functionalization, and are unable to react with the AAROP reaction medium components. Table 1 shows the designations of the samples produced, the polymerization yield, and the real load (R_L) content determined by thermogravimetric analysis (TGA), according to Equation (6):

$$R_L = R_f - R_{PA6}, \% \quad (6)$$

where R_{PA6} and R_f represent the carbonized residues of the empty MPs and the Me-MPs at 600 °C, respectively. It is important to note that during AAROP all MP samples underwent solid-state crystallization for 2 h at 130–135 °C, under constant stirring at 800 rpm. The purification and drying procedures were also the same.

Table 1. Designation, composition, and polymerization yields of MP samples.

Sample Designation	Load [wt.%] ^(a)	Composition ^(b) , [vol.%]		Yield ^(c) [wt.%]	Real load ^(d) [wt.%]
		Metal	PA6		
PA6	-	0.0	100.0	56.0	-
Al10	10	9.2	90.8	45.1	19.4
Cu10	10	2.6	97.4	48.6	17.6
Mg10	10	8.8	91.2	48.9	16.5

^(a) Based on the weight of ECL in the starting AAROP mixture; ^(b) based on the volumes of metal and PA6 in the respective sample; ^(c) calculated as a relation the MP final weight the sum of ECL plus metal filler weights; ^(d) determined by TGA according to Equation (6).

As seen from the SEM micrographs in Figure 1a–c, each metal filler is composed of particles with specific sizes and shapes that determine, to a great extent, the morphology of the respective hybrid Me-MP.

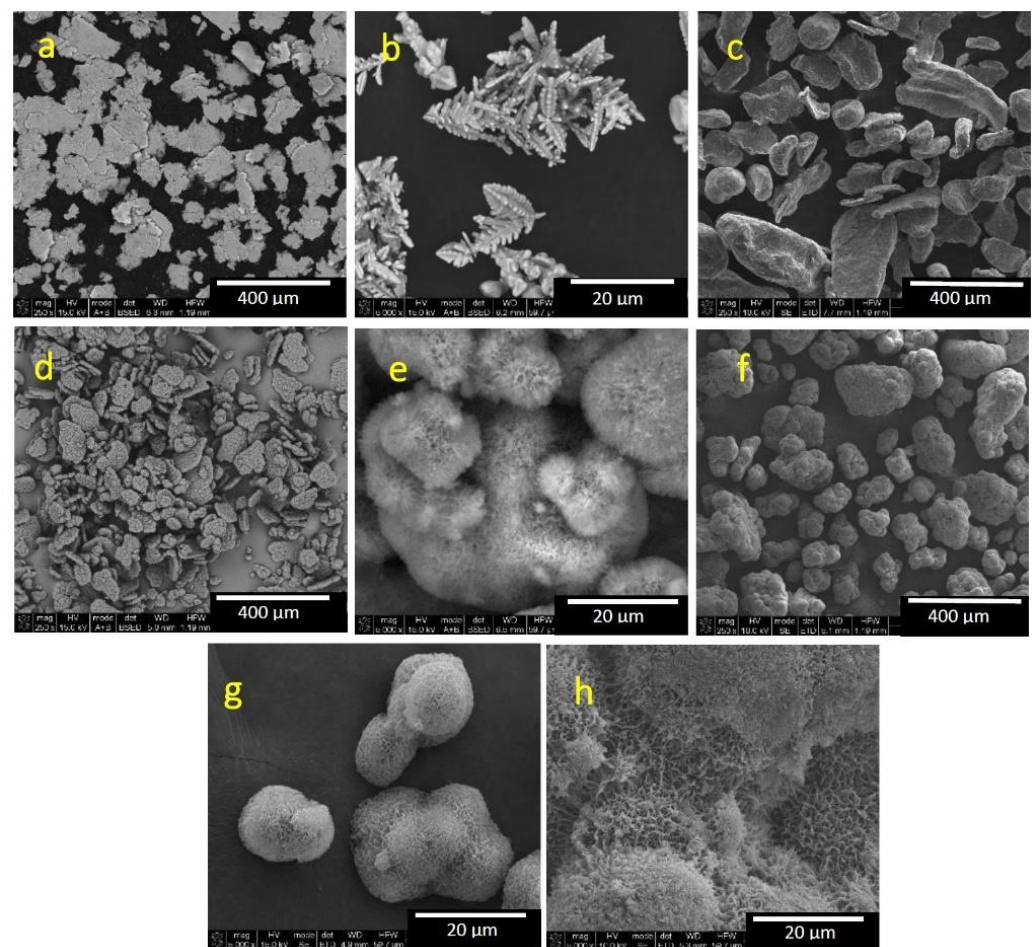


Figure 1. SEM micrographs of neat metal particles and Me-MPs: (a) Al; (b) Cu; (c) Mg; (d) Al10; (e) Cu10; (f) Mg10; (g) PA6; (h) close view of Mg10. For sample designations see Table 1.

In the case of the Al10 sample (Figure 1d), most of the hybrid microparticles are single Al platelets with a length of ca.100 µm, coated by PA6. The Cu10 MP (Figure 1e)

represents aggregates with d_{max} of ca. 30 μm , comprising several partially fused spheroids with typical diameters of $\geq 10 \mu\text{m}$. The Mg10 sample (Figure 1f) displays large irregular particles, with a broad size distribution between 50–300 μm . All MPs seem to contain one or more metal particles inside a PA6 shell that encapsulates the metal load. Moreover, all hybrid microparticles in Figure 1 display certain porosity of the PA6 shell, best observed in Figure 1g,h, showing the neat PA6 MP and magnification of the Mg10 sample. It should be noted that the conventional extruder mixing of polymer granulates with metal powders, and the subsequent grinding for ssNMR sample preparation, cannot produce such a morphology characterized by dense packing of the metal filler within a shell of the matrix polymer. All of these structural peculiarities will be taken into consideration in the ssNMR data interpretation.

3.2. Characterization by ssNMR

For the metal-loaded MP in this work obtained via AAROP in solution, only a small effect of the magnetic field created within the metal particles can be anticipated upon the PA6 matrix material, given that the metals are not chemically bonded to PA6. Theoretically, the influence on the ^{13}C ssNMR resonances is expected to be restricted to the PA6 carbons in close vicinity of the metal filler particles, resulting in signal broadening, magnetic field shifts, and relaxation enhancement. Therefore, the ssNMR experiments were designed in such a way that it would be possible to register and assess these three effects.

3.2.1. General Evaluation of the ssNMR Spectra

Figure 2a shows the ^{13}C MAS and Figure 2b shows the ^{13}C CP/MAS spectra of Me-MP samples. The respective ^{13}C chemical shifts are presented in Table 2. Figure 2b also presents the PA6 chemical structure with the numbering of the C nuclei. The MAS spectra were obtained under the Bloch decay conditions with a short time between two consecutive scans (See the Experimental Section, characterization by ssNMR, experiment (i)). This procedure mostly displays the signals of the amorphous PA6 fraction, since the spin system of the crystalline domains does not have sufficient time for relaxation, and their signals are not registered. The spectra recorded by ^{13}C CP/MAS with long periods of time between two consecutive scans (experiment (ii)) reveal a weighted superposition of the signals from both crystalline and amorphous domains, which permits quantification of the two phases.

Table 2. ^{13}C MAS and ^{13}C CP/MAS chemical shifts in C nuclei obtained from MP samples. The average error of the chemical shift determination is ± 0.2 ppm.

Sample and ssNMR Experiment		Chemical Shift δ , ppm				
		C1	C2 + C3	C4	C5	C6
PA6	MAS	- ^a	27.8	- ^a	36.2	173.5
	CP/MAS	42.8	29.7	26.0	36.2	172.8
Al10	MAS	- ^a	28.1	- ^a	37.1	174.7
	CP/MAS	42.7 ^b	29.4 ^b	- ^a	36.6 ^b	174.1
Cu10	MAS	- ^a	27.9	- ^a	36.8	174.5
	CP/MAS	43.4	30.3	26.4	36.6	173.6
Mg10	MAS	- ^a	28.0	- ^a	35.6	173.5
	CP/MAS	42.5	29.7	- ^a	36.4	173.0

^a Unresolved; ^b Broad signal.

From Figure 2a,b, the ^{13}C MAS and CP/MAS ssNMR spectra of PA6 consist of four signals, attributable to (in ascending order of δ , ppm) C4, C2 + C3, C5, and C1 nuclei in the methylene groups region and one peak assigned to the C6 carbonyl nucleus. The chemical shifts of the six magnetically nonequivalent PA6 carbons are shown in Table 2, and are identical or close to those reported earlier for PA6 [15,16]. In particular, the signals at about

42 and 36 ppm are assigned to C1 and C5 in the α -PA6 polymorph, respectively, which indicates that PA6 MP contains predominantly α -PA6 crystallites [15].

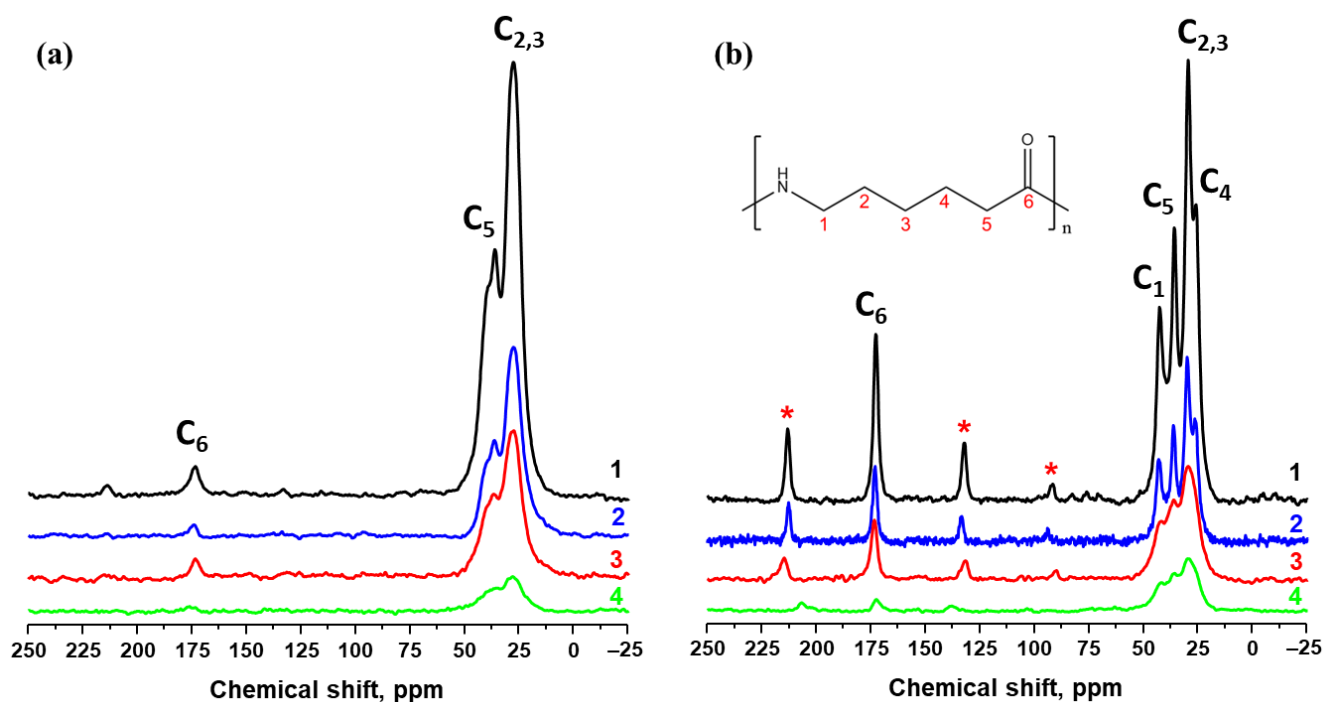


Figure 2. Full ssNMR spectra comparison of Me-MP samples at room temperature: (a) ^{13}C MAS and (b) ^{13}C CP/MAS. 1—PA6, 2—Cu10, 3—Al10, 4—Mg10. Asterisks denote spinning sidebands.

Comparing the MAS and CP/MAS spectra of empty and Cu-loaded PA6 MPs (Figure 2a,b, curves 1 and 2) reveals the similarity of the PA6 resonance lines, as far as peak position and resolution are concerned. The Cu filler is diamagnetic with negative magnetic susceptibility $\chi = -1.0 \times 10^{-5}$, which results in an unperturbed system in the presence of a magnetic field. Thus, the fact that this load does not obstruct the observation of the matrix NMR peaks was expected. Moreover, Cu10 is the MP system with the smallest volumetric loading, 2.6%, meaning that most of the polymer matrix is not in close contact with the metal filler. This makes the effect of Cu on the PA6 NMR signals position and resolution even less detectable.

Curves 1 and 2 in Figure 2a,b also show a clear decrease in the intensity of the signals of the Cu10 sample compared to the neat PA6. This effect has to be related to radio frequency (RF) absorption, due to the skin effect characteristic of conventional conductors. The skin depth is inversely proportional to the square root of the conductivity and the pulse frequency. For the neat Cu metal, it ranges from 8.61 mm to 2.11 μm for frequencies from 60 Hz to 109 Hz, respectively [34]. In the case of metal-loaded MP, however, the conductivities σ_{dc} of neat PA6 and all metal-loaded loaded MP samples was found to be in the range of 10^{-11} – 10^{-9} S/m [27,35]. Evidently, the Me-MPs retain the electrical insulating properties of the neat PA6 matrix, meaning that within the concentration range studied (2–9 vol.%), percolation between the metal particles was not achieved. On the other hand, as was demonstrated by SEM in Figure 1, the metal particles in MP are completely encapsulated within the PA6 shell. At the ^{13}C resonance frequencies used in the present study, the skin depths for Cu as bulk metal are about 8 μm , i.e., less than the Cu filler particles' average sizes (20–40 μm). This leads to RF power loss and the observed drop in the ssNMR signal intensity of the Cu10 sample.

Regarding the Al10 or Mg 10 samples carrying ca. 9 vol.% of paramagnetic payloads (Figure 2, curves 3 and 4), line broadening and loss of peak resolution in both MAS and CP/MAS signals were observed as compared to neat PA6. These effects are in good

agreement with the basic theory explaining the influence of paramagnetic metals upon the NMR signals' intensity and width, both in solution and in solid-state [36].

Figure 3a,b separately display the evolution of the C1–C5 signals' intensity and shape in the MAS and CP/MAS spectra of neat and Me-MPs. The evolution of the C6 signal intensity and the shape of all samples are displayed in Figure 3b,c. The chemical shifts of all peaks are presented in Table 2.

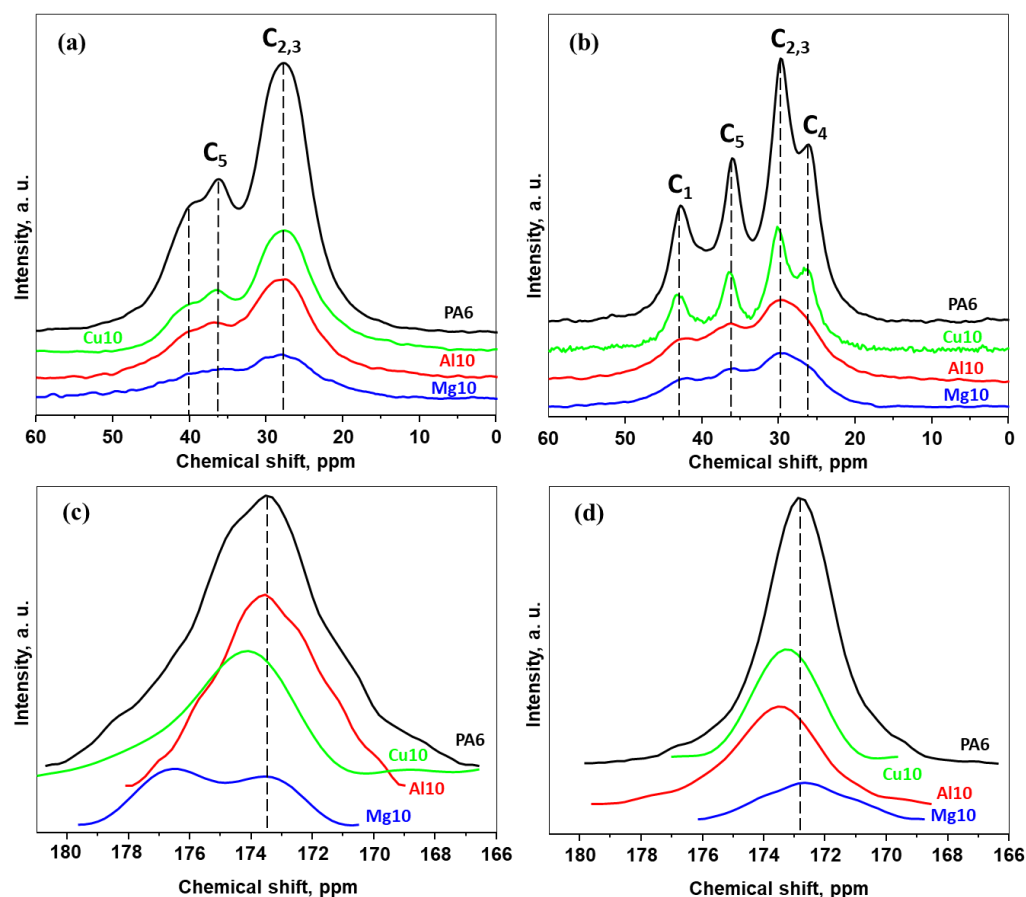


Figure 3. Evolution of the shape and position of the ssNMR signals as a function of the metal filler in ^{13}C MAS (left) and ^{13}C CP/MAS (right) with neat PA6 and Me-MP samples: (a,b)—C1–C5 signals; (c,d)—C6 signal. The curves are displaced along the Y-axis, whereby each set of curves has the same scaling of intensity.

As can be seen in the MAS spectra in Figure 3a,c, the incorporation of metal particles into PA6 leads to a notable decrease in the intensity of the ssNMR methylene C-signals and line broadening. In the Mg10 sample, the C6 signal was split into two, whereby a second peak appeared in weaker fields at ≈ 177 ppm. Analyzing the differences in the resonance lines of the aliphatic carbons in the CP/MAS experiment (Figure 3b,d) reveals that the presence of metal particles in the matrix led to a similar intensity decrease in well-expressed and line broadening of the methylene PA6 peaks in the Al10 and Mg10 samples. Regarding the carbonyl C-signal (Figure 3b), its intensity drops significantly for all samples; this can be best observed in the Mg10 sample. While all effects of intensity increase, and line broadening in MAS or CP/MAS spectra are to be related to the diamagnetic or paramagnetic properties of the metal fillers, the splitting of the C6 signal in the MAS of sample Mg10 is difficult to explain, undoubtedly because of the insufficient signal-to-noise ratio in this spectrum.

3.2.2. Influence of the Metal Particles on the Crystalline Structure of the PA6 Matrix

The second step in the evaluation of the PA6 crystalline structure in the Me-MP series by ssNMR was the determination of their degree of crystallinity, X_c^{ssNMR} , as a function of the metal type. The procedure uses only spectral data from aliphatic carbons based on the assumed comparable C-H CP efficiency for CH₂ groups located in amorphous and crystalline regions. Such an assumption is confirmed in the next section by showing that these domains present similar mobility in the kHz frequency range.

First, the MAS spectra were deconvoluted in order to obtain only the response of the amorphous PA6 domains. Then, the CP/MAS spectra were deconvoluted, including the data from MAS in the input parameters and considering them as the response of the amorphous phase. The deconvolution was performed using Gaussian functions to fit both MAS and CP/MAS spectral lines. Apart from calculating X_c^{ssNMR} , the data from MAS and CP/MAS spectra deconvolution were used to quantify the effect of the metal particles on the width as well as the chemical shift in the signals of the PA6 MP shell. Figure 4 shows the deconvolution of the experimental MAS spectra (the black dots) fitted by Gaussian peaks, as well as the resulting reconstructed spectra (the green solid lines). The numeric data obtained from the fits of all MP spectra are displayed in Table 3.

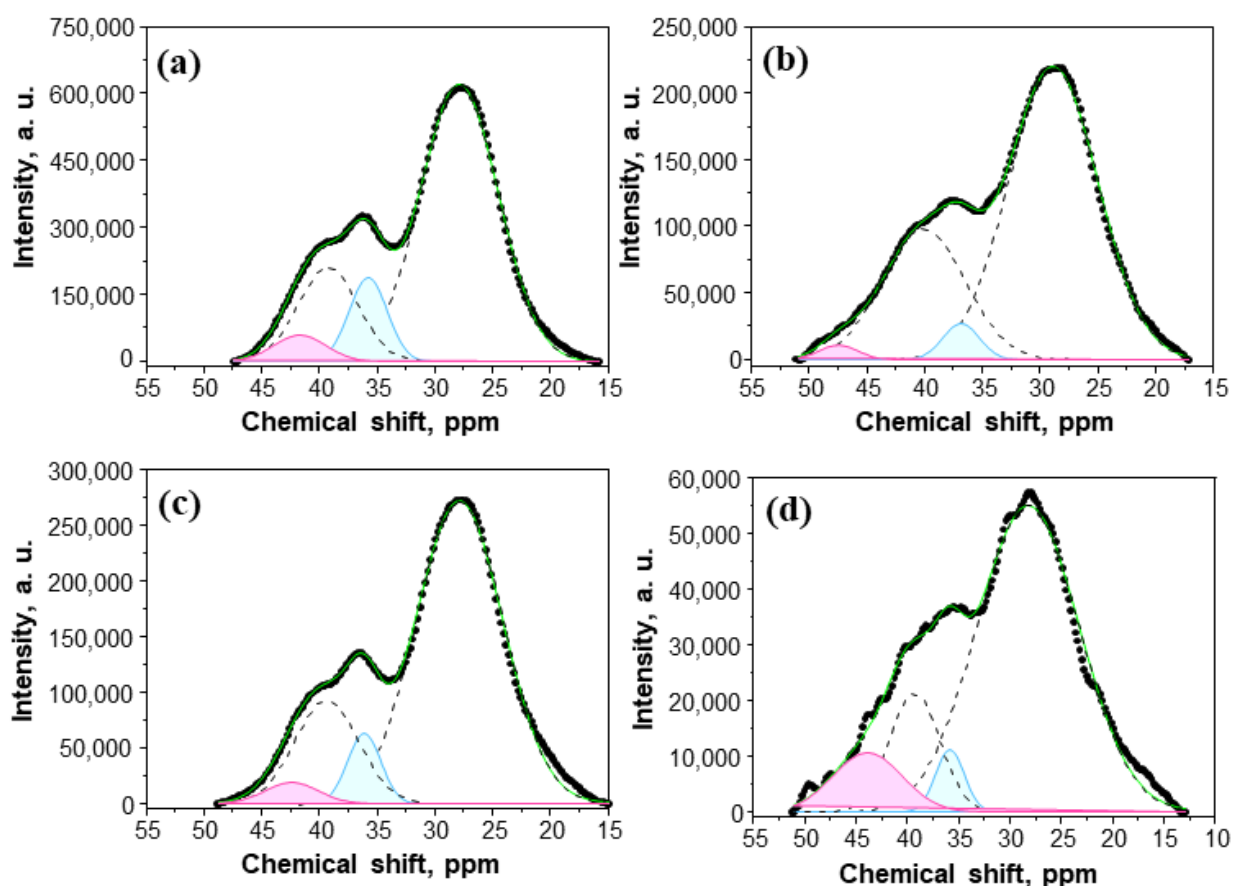


Figure 4. Aliphatic region of the ¹³C MAS spectra of: (a) neat PA6, (b) Al10, (c) Cu10, and (d) Mg10. The two dashed curves represent the combination of the resonances (C4, C2 + C3) and (C1 + C5) from the amorphous regions. The peaks shaded in blue and pink areas represent the C5 and C1 signals, respectively, located in more ordered domains. The chemical shifts of all resonance lines are tabulated in Table 3.

Regarding the amorphous regions, the first conclusion from Figure 4 and Table 3 is that the merged resonance peak of (C1 + C5) in all studied samples is centered at ca. 39.3 ppm, i.e., it is downfield shifted with respect to the (C4, C2 + C3) peak appearing at ca. 28 ppm. This shift of the (C1 + C5) resonances to lower fields is expected, and it is due

to the unshielding of these nuclei caused by their closer vicinity to NH and C=O groups, respectively. Weak downfield shifts of up to 0.40 ppm are observed with these two peaks in the presence of metal particles, the larger one being assigned to the (C4, C2 + C3) combined resonance. This means that the metal particles in the amorphous PA6 phase interact only slightly with the CH₂ groups of the PA6 shell, not causing significant redistribution of the electron density of the respective C-atoms.

Table 3. ¹³C MAS results of the MP samples obtained by peak fitting of ssNMR data for the aliphatic region. The bolded values correspond to resonances related to the more ordered phase. All variations are with respect to the signals of the PA6.

Sample (Fitting Coef.)	Carbon	Chemical Shift, ppm	Variation of Chemical Shift, ppm	FWHM, ppm	Variation FWHM, ppm
PA6 (0.9986)	C4, C2 + C3	27.9 ± 0.1	-	8.01	-
	C5 ^(a)	35.8 ± 0.4	-	3.88	-
	C1, C5	39.3 ± 0.2	-	6.12	-
	C1 ^(b)	41.6 ± 0.2	-	5.36	-
Al10 (0.9986)	C4, C2 + C3	28.2 ± 0.1	0.3	9.15	1.14
	C5 ^(a)	36.1 ± 0.1	0.3	3.75	-0.13
	C1, C5	39.3 ± 0.3	0.0	8.42	2.30
	C1 ^(b)	46.7 ± 0.2	5.1	4.01	-1.35
Cu10 (0.9965)	C4, C2 + C3	27.9 ± 0.1	0.0	8.86	0.85
	C5 ^(a)	36.1 ± 0.3	0.3	3.40	-0.48
	C1, C5	39.4 ± 0.4	0.1	6.53	0.41
	C1 ^(b)	42.4 ± 0.2	0.8	5.48	0.12
Mg10 (0.9918)	C4, C2 + C3	28.3 ± 0.1	0.4	11.72	3.71
	C5 ^(a)	35.9 ± 0.3	0.1	3.29	-0.59
	C1, C5	39.3 ± 0.6	0.0	5.76	-0.36
	C1 ^(b)	43.8 ± 0.5	2.2	7.99	2.63

^(a) C5 nucleus in close vicinity to C=O in more ordered PA6 domains; ^(b) C1 nucleus in close vicinity to NH in more ordered domains.

It should be noted that not all MAS spectra in Figure 4 can be fitted appropriately without introducing two additional narrow peaks (i.e., related to the PA6 phase with some order) at ca. 36 ppm and in the 42–47 ppm interval, attributable to C5 and C1 resonances, respectively. The appearance of these two peaks can be explained by the formation of H-bonds involving carbonyl and secondary amine groups, leading to some incipient ordering in the amorphous phase. As a result, a redistribution of the electron density around C1, C5, and C6 nuclei occurs, resulting in the downfield shift in the corresponding resonances. The formation of multiple intra- and intermolecular H-bonds should result in some densification of the amorphous fraction, forming some quasi-ordered (or rigid amorphous) PA6 phase [36]. The latter produces the relatively narrow C1 and C5 peaks that can be revealed in a ¹³C MAS ssNMR experiment. The introduction of Al and Mg particles in MPs results in a significant downfield shift of the C1 signal of the PA6 shell by 5.1 and 2.2 ppm, respectively, while in the presence of Cu, the shift is 0.8 ppm, which is statistically significant (Table 3). The shift of the C5 signal with respect to that of the neat PA6 is only 0.1–0.3 ppm, i.e., within the margin of the experimental error. It seems that the C1-nucleus, which is close to the N-H group in the PA6 shell, is more sensitive to the presence of metal loads than the C5 directly bonded to the C=O group.

Regarding the full width at half maximum (FWHM) of all peaks in the MAS experiment (Table 3), in the presence of metals, most of the PA6 peaks become broader. The exact

values of FWHM variation, however, should be treated with caution due to the possibility of signal overlapping unaccounted for in the deconvolution procedure.

The deconvolution of the ^{13}C CP/MAS spectra (Figure 5, Table 4) allows the distinction between the methylene C-signals related to the amorphous and the crystalline domains of Me-PA6 MPs. The chemical shifts of all peaks, in both amorphous and crystalline domains, do not change significantly due to the presence of metal particles. However, once again, all peaks in neat PA6 and Cu10 samples are similar in shape, while the C-resonances in the Al10 and Mg10 become broader (see Column 6 of Table 4). The FWHM increase in these samples is larger for the crystalline phase (between 0.7 ppm and 3.9 ppm), while it remains around 1 ppm for the methylene C signals from amorphous domains. This means that both Al and Mg particles more strongly influence the C nuclei in the crystalline phase. More precisely, the increase in FWHM in Al10 is in the range of 1.2 ppm (C1) to 3.8 ppm (C5), and between 3.2 ppm (C1) and 2.6 ppm (C5) for Mg10. On the other hand, the FWHM is either unchanged or slightly decreased in the presence of Cu particles. Therefore, the effect of paramagnetic Al and Mg and diamagnetic Cu on the FWHM variation is similar in ^{13}C CP/MAS and MAS spectra.

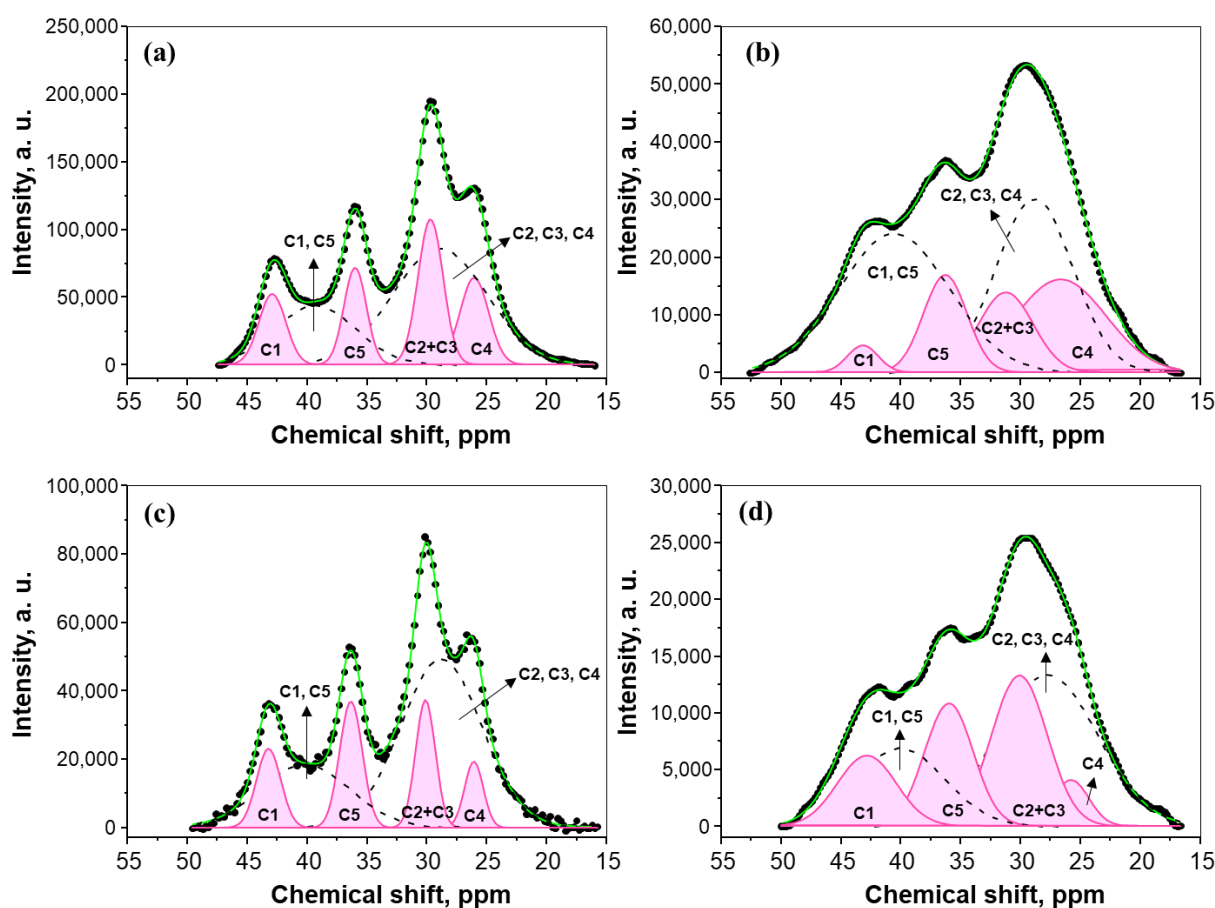


Figure 5. Aliphatic region of the ^{13}C CP/MAS spectra of: (a) neat PA6 and such loaded (b) Al10, (c) Cu10, and (d) Mg10 PA6 MP: experimental (black dots) and computed (green line) spectra. The pink-shaded Gaussians represent the peaks of the indicated carbons in the crystalline regions, and the black dashed lines are the curves used to deconvolute the signal from amorphous domains (see Figure 4). Table 4 contains the identification and quantification of all resonance lines in this figure.

Table 4 also presents the degree of crystallinity obtained from CP/MAS data. The $X_c^{ssNMR}_{total}$ value represents the contribution of the C-aliphatic peaks from the crystalline domains (Equation (2)), while for the calculation of the $X_c^{ssNMR}_{partial}$, the contribution of

the peaks from the amorphous regions is also accounted for (see Equation (1), Experimental Section).

Table 4. ^{13}C CP/MAS results for the aliphatic region. The carbons in boldface are those of the crystalline PA6 phase.

Sample (Fitting Coef.)	Carbon	Chemical Shift, ppm	Variation of Chemical Shift, ppm	FWHM, ppm	Variation FWHM, ppm	Area, %	$X_c^{ssNMR\ part}$, % (a)	$X_c^{ssNMR\ total}$, % (b)	X_c^{DSC} , % (c)	X_c^{XRD} , %
PA6 (0.9995)	C4	26.0 ± 0.1	-	2.83	-	9.70	35.86	39.4	39.4	44.5
	C2, C3, C4	28.9 ± 0.2	-	9.29	-	42.38				
	C2 + C3	29.7 ± 0.0	-	2.45	-	14.00				
	C5	36.0 ± 0.0	-	2.19	-	8.39				
	C1, C5	39.2 ± 0.2	-	7.87	-	18.22				
	C1	42.9 ± 0.0	-	2.63	-	7.31				
Al10 (0.9996)	C4	27.5 ± 0.9	1.5	5.73	2.90	15.38	46.45	49.9	52.2	50.7
	C2, C3, C4	28.3 ± 1.6	-0.6	10.6	1.27	29.99				
	C2 + C3	30.8 ± 0.3	1.1	4.18	1.72	10.63				
	C5	36.3 ± 0.8	0.3	6.05	3.85	20.13				
	C1, C5	42.3 ± 2.7	3.1	9.41	1.54	20.11				
	C1	42.7 ± 0.2	-0.2	3.83	1.20	3.76				
Cu10 (0.9980)	C4	26.1 ± 0.0	0.1	1.84	-0.99	11.44	43.90	46.7	42.7	49.5
	C2, C3, C4	28.8 ± 0.1	-0.1	7.92	-1.37	35.11				
	C2 + C3	30.1 ± 0.0	0.4	1.93	-0.52	16.04				
	C5	36.3 ± 0.0	0.3	2.21	0.02	10.29				
	C1, C5	40.0 ± 0.4	0.8	8.82	0.95	18.25				
	C1	43.2 ± 0.0	0.3	2.28	-0.25	8.87				
Mg10 (0.9993)	C4	25.8 ± 0.3	-0.2	3.49	0.66	3.92	39.78	47.7	53.2	49.8
	C2, C3, C4	27.8 ± 4.7	-1.1	9.94	0.65	35.96				
	C2 + C3	30.0 ± 1.0	0.3	5.47	3.02	19.84				
	C5	36.0 ± 0.4	0.0	4.78	2.59	14.15				
	C1, C5	40.0 ± 3.4	0.8	8.77	0.91	16.36				
	C1	42.8 ± 3.8	-0.1	5.79	3.16	9.78				

(a) Calculated according to Equation (1); (b) calculated according to Equation (2); (c) determined from DSC data according to Equation (5); for XRD data deconvolution and X_c^{XRD} calculation, see Figure S3 in the SM and Ref. [22].

The values of the degree of crystallinity, determined by DSC, X_c^{DSC} and by synchrotron XRD, X_c^{XRD} , are also shown in Table 4 in order to enable comparison with the NMR data. Figure S2 and Table S1 in the SI present the thermograms and the numeric data, respectively, as obtained by DSC. Figure S3 exemplifies the deconvolution of the XRD one-dimensional pattern of Mg10 MP. More information about this procedure has been presented in earlier structural studies on PA6 [22].

From the results in Table 4 regarding the two $X_c^{ssNMR\ partial}$ values of all samples, it can be concluded that the one considering the three central methylene carbons (i.e., C2 + C3 + C4) is always lower than the one based on the C1 + C5 carbons. This is an indication that the C1 and C5 carbons, located next to the NH and C=O groups that participate in the H-bond formation, may be a part of a more ordered PA6 phase, while the C2-C4 carbons are included in the more disordered domains. The X_c^{XRD} data are similar to the $X_c^{ssNMR\ partial}$ calculated from the (C1 + C5) signals. It is well known that the XRD method probes all domains with some order, i.e., X_c^{XRD} cannot distinguish between the contributions of the rigid amorphous phase and the crystalline phase. On the other hand, the $X_c^{ssNMR\ total}$ values are more similar to the X_c^{DSC} , the differences being less than 5%. In principle, a total coincidence between the crystallinities determined by ssNMR, XRD, and DSC should not be expected, since the principles behind these analytical methods are different. However, the presence of some relations between the different data sets is an indirect indication of the correctness of the ssNMR deconvolution procedure employed.

It is important to note that crystallization of PA6 occurs in the process of AAROP, in which the polymerization parameters are kept exactly the same for all MP samples (see the Experimental Section). Hence, the differences in their crystalline structure should only be related to the presence of different metal fillers.

3.2.3. Molecular Dynamics Studies by ssNMR

In addition to the information on the Me-MP crystallinity, ssNMR was used to produce time-dependence data suitable for studying molecular dynamics. As shown by Schreiber et al. [36], the distinction between mobile (disordered) and rigid (ordered) PA6 fractions appears to be best achieved by using ${}^C T_{1\rho}$; therefore, it was also evaluated in the present study. In addition, this study reports on ${}^C T_1$ evaluation. The ${}^C T_{1\rho}$ (ms) and ${}^C T_1$ (s) obtained from the carbon nuclei C1–C6 nuclei are shown in Figure 6a,b, respectively. Table S2 displays the corresponding numeric data.

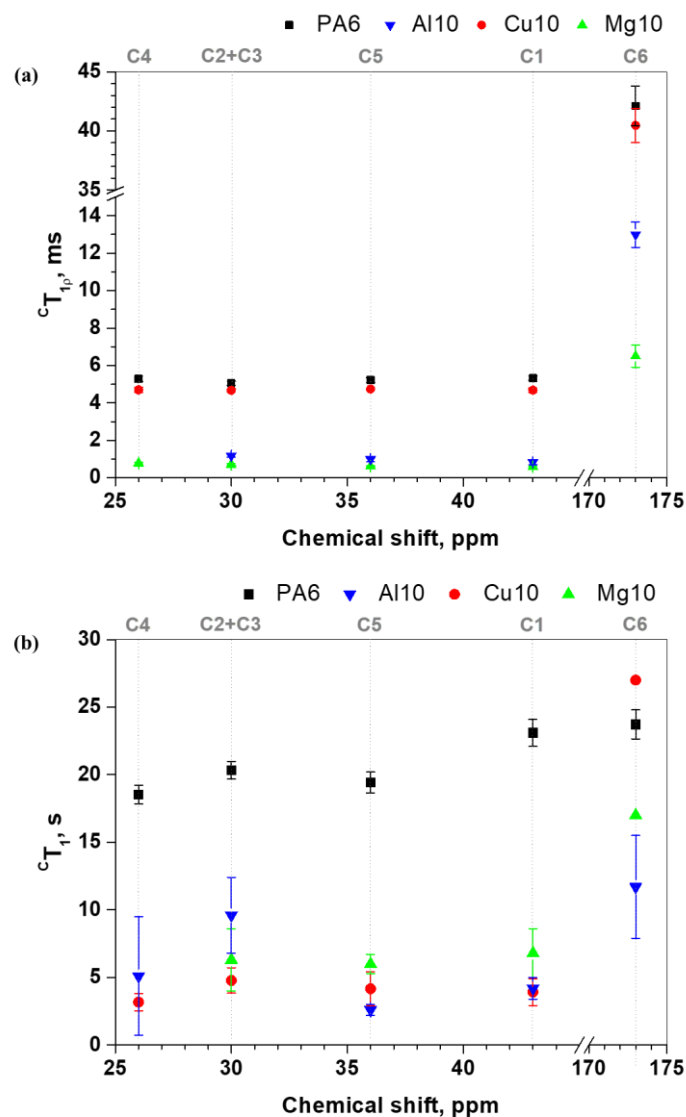


Figure 6. (a) ${}^C T_{1\rho}$ and (b) ${}^C T_1$ of the carbon nuclei in empty and Me-MP samples.

The ${}^C T_{1\rho}$ data for neat PA6 MP was best obtained from mono-exponential fitting functions (Equation (3) in the Experimental Section), showing that, in this polymer, the amorphous and rigid domains presented similar mobility in the kHz frequency range.

The aliphatic carbons are characterized by ${}^C T_{1\rho}$ of about 5 ms, and a longer relaxation time can be observed for carbonyl ${}^{13}\text{C}$ O (about 42 ms), which is characteristic of an ordered (rigid) phase [36]. The significant difference between aliphatic and carbonyl data is due to C-H dipole–dipole interaction, being dominant for ${}^{13}\text{C}$ in methylene groups. On the other hand, carbonyl groups participate directly in H-bonds, and ${}^{13}\text{C}$ has a large shielding anisotropy, which also contributes to the nucleus relaxation (easily detected by the presence

of spinning sidebands at low MAS rate, not completely averaging out that interaction, as seen in Figure 2b).

NMR investigations of orientational and structural changes in PA6 undrawn samples reported about 55 ms and 3 ms on ${}^C T_{1\rho}$ of ${}^{13}\text{C}$ in rigid and mobile phases [36]. The ${}^C T_{1\rho}$ of C6 in PA6 MP and Cu10 MP is in the range of 40.5 ± 1.4 ms (Cu10) to 42.1 ± 1.7 ms (PA6); therefore, these data are very close to those on rigid domains in neat, non-oriented PA6 [36]. The ${}^C T_{1\rho}$ for the aliphatic nuclei of PA6 MP and Cu10 MP is close to 5.0 ms; that is, in both samples, all aliphatic nuclei have similar mobility.

Concerning the Al10 and Mg10 samples, intense mobility is registered, with ${}^C T_{1\rho}$ values in the range of 0.58–0.99 ms and 6.50–12.99 ms for the carbonyl group. These findings suggest that the Al and Mg filler particles interact more strongly with carbon nuclei. The observed decrease in ${}^C T_{1\rho}$ should be attributed to the proximity of paramagnetic particles to carbon nuclei. Additionally, the Al and Mg metal particles may upset the order in the PA6 domains, thus facilitating the mobility of the C atoms. These results agree with the line shape of the respective ${}^{13}\text{C}$ MAS and ${}^{13}\text{C}$ CP/MAS spectra (Figure 2), where broader signals and low resolution were observed [37].

The data from ${}^C T_1$ measurements (Figure 6b, Table S2) show that the presence of metal particles decreases the ${}^C T_1$ of the aliphatic nuclei as compared to neat PA6. In the PA6 sample, the ${}^C T_1$ values of the aliphatic C (from mono-exponential fitting functions) are from about 18.5 ± 0.7 s (C4) to 23.1 ± 1.0 s (C1), while in Me-MPs, such values are notably lower, from about 2.6 ± 0.4 s (C5 of Al10) to 9.6 ± 2.8 s (C2,3 of Al10). Therefore, the presence of metal particles affects the segmental motion of the PA6 chains, intensifying the spin–lattice relaxation of the aliphatic C, independently of the metal load. The similarity between the aliphatic ${}^C T_1$ values in Me-MPs may be due to the influence of spin-diffusion [38], which can hide other properties of the materials under study.

Table S2 (rows 2 and 3) also includes PA6 and Cu10 ${}^C T_1$ data obtained from double-exponential fitting functions (Equation (4)), as should be expected for a semicrystalline polymer such as PA6. Contribution percentages of fast and slow components, assigned to amorphous and crystalline regions, respectively, are also indicated. Although some values need to be considered as rough estimates, due to large associated fitting errors, it is worth mentioning the similar behavior of PA6 and Cu10 samples. As for Al10 and Mg10, the low spectral signal-to-noise ratios did not allow an identical procedure to be followed.

Concerning the C6 nucleus (Figure 6, Table S2), contrary to the analysis of ${}^C T_{1\rho}$, the effect of the carbonyl group on the spin–lattice relaxation is less visible. However, differences can be observed between the analyzed samples. Long T_1 time is related to the crystalline phase [38], and it agrees well with the line narrowing of the ${}^{13}\text{C}$ CP/MAS spectra of the empty and Cu-loaded MP (Figure 2b). On the other hand, broader signals indicate the predominance of the amorphous phase and the consequently lower T_1 values, which match with the ${}^C T_1$ values obtained for C6 in Al- and Mg-loaded MP (Table S2) and the respective ${}^{13}\text{C}$ CP/MAS spectra (Figure 2b). Thus, apparently, the hydrogen bonding characteristic for the formation of PA6 crystallinity is somehow absent at short-range order, probed by ssNMR in the Al10 and Mg10 samples, with the consequent increase in carbonyl mobility, resulting in the lower ${}^C T_1$ values of the C6. However, because Al10 and Mg10 present a higher degree of crystallinity than neat PA6 and Cu10 samples (Table 4), such a T_1 decrease can only be attributed to the proximity of paramagnetic metals to C6 nuclei, as pointed out for the observed ${}^C T_{1\rho}$ decrease.

4. Conclusions

In summary, this work presents a ${}^{13}\text{C}$ ssNMR study on the crystalline structure and molecular dynamics in empty and metal-loaded PA6-based MPs obtained by AAROP in solution. The ${}^{13}\text{C}$ MAS and ${}^{13}\text{C}$ CP/MAS experiments revealed a spectral similarity between neat PA6 and Cu10 samples, on one hand, and between Al10 and Mg10, on the other. The spectra of the Al- and Mg-loaded MP display lines broadened and had low peak resolution due to the paramagnetic properties of the metals. These effects were not

observed in the Cu10 sample, in which the dispersion of Cu particles and their diamagnetic properties did not significantly affect the C resonances of the PA6 matrix.

^{13}C CP/MAS spectra are not commonly used to quantify crystalline and amorphous components due to the C-H CP efficiency dependence; instead, although requiring long acquisition times, direct-excitation measurements with long enough recycle time delays are preferred. As seen from the similar values of the crystallinity indices obtained by three independent methods (ssNMR, DSC, and XRD), the ssNMR spectral data from aliphatic carbons (using CP/MAS and direct-excitation under MAS measurements) allowed for the correct determination of the MP samples' crystallinity. The latter seems to be dependent on the size and morphology of the dispersed metal fillers, which also act as nucleating agents during solid-state crystallization by the end of AAROP.

The molecular dynamics study showed that the local mobility of each C nucleus is influenced by the presence of the metal particles. The paramagnetic properties of the large Al and Mg particles lower the $^{\text{C}}T_{1\rho}$ and $^{\text{C}}T_1$ spin–lattice relaxation times of both aliphatic and carbonyl carbon nuclei. On the other hand, as the dendritic-shaped, relatively small, and diamagnetic Cu particles do not change $^{\text{C}}T_{1\rho}$, it may be concluded that in the kHz frequency range selected, the local motion in Cu10 and PA6 MP samples is similar.

All of these results may be useful in the development of polyamide-based microparticles, with customized properties carrying metal or mixed metal/carbon allotrope payloads applicable for the preparation of flexible EMI materials.

Supplementary Materials: The following supporting information can be downloaded at: <https://www.mdpi.com/article/10.3390/cryst12111579/s1>, Figure S1: Chemical reactions occurring during AAROP of ϵ -caprolactam ($\text{R}^1 = (\text{CH}_2)_5$) to neat PA6 MP. The active substance of the AAROP activator is designated as C20; the chemical structure of the AAROP initiator dicaprolactamato-bis-(2-methoxyethoxy)-aluminate (DL) is presented wherein $\text{R} = \text{OCH}_2\text{CH}_2\text{OCH}_3$; Figure S2: DSC thermograms of empty and Me-MPs in N_2 atmosphere: (a) first heating scan, (b) recrystallization from the melt, (c) second heating scan. For sample designation, please see Table 1 of the main manuscript; Figure S3: Example showing the result of deconvolution of WAXS pattern of sample Mg10. All WAXS patterns are obtained at 30°C with the pulverulent MP samples as explained in the Experimental Section; Table S1: DSC data of empty and Me-MP samples; Table S2: $^{\text{C}}T_{1\rho}$ (ms) and $^{\text{C}}T_1$ (s) of the empty and Me-MPs; the relaxation times were obtained by fitting the experimental data with mono-exponential functions (Equation (3)), unless specified otherwise.

Author Contributions: Conceptualization, T.G.N. and Z.Z.D.; methodology, T.G.N.; software, T.G.N.; validation, N.V.D. and T.G.N.; formal analysis, F.M.O., T.G.N. and N.V.D.; investigation, F.M.O. and N.V.D.; data curation, F.M.O.; writing—initial draft preparation, F.M.O.; writing—review and editing, Z.Z.D., N.V.D. and T.G.N.; supervision, Z.Z.D. and T.G.N.; funding acquisition, Z.Z.D. and N.V.D. All authors have read and agreed to the published version of the manuscript.

Funding: This research was funded by *Fundação para a Ciência e Tecnologia* (FCT), project UID/CTM/50025/2019. N. Dencheva is also grateful for the personal program contract CTTI-51/18-IPC. FMO wishes to thank the AdvaMTech—Ph.D. Program in Advanced Materials and Processing for the Ph.D. grant PD/BD/114372/2016 (FCT).

Data Availability Statement: The data presented in this study are available on request from the corresponding author.

Conflicts of Interest: The authors declare no conflict of interest.

References

1. Tomasini, A.; León-Santesteban, H.H. 12—Nylon uses in biotechnology. In *Biocomposites*; Misra, M., Pandey, J.K., Mohanty, A.K., Eds.; Woodhead Publishing Series in Composites Science and Engineering; Woodhead Publishing: Cambridge, UK, 2015; pp. 319–346. ISBN 978-1-78242-373-7.
2. Schmidt, J.; Sachs, M.; Fanselow, S.; Zhao, M.; Romeis, S.; Drummer, D.; Wirth, K.-E.; Peukert, W. Optimized polybutylene terephthalate powders for selective laser beam melting. *Chem. Eng. Sci.* **2016**, *156*, 1–10. [[CrossRef](#)]
3. Schmidt, J.; Sachs, M.; Blümel, C.; Winzer, B.; Toni, F.; Wirth, K.-E.; Peukert, W. A novel process route for the production of spherical LBM polymer powders with small size and good flowability. *Powder Technol.* **2014**, *261*, 78–86. [[CrossRef](#)]

4. Wang, G.; Wang, P.; Zhen, Z.; Zhang, W.; Ji, J. Preparation of PA12 microspheres with tunable morphology and size for use in SLS processing. *Mater. Des.* **2015**, *87*, 656–662. [[CrossRef](#)]
5. Drummer, D.; Medina-Hernández, M.; Drexler, M.; Wudy, K. Polymer Powder Production for Laser Melting Through Immiscible Blends. *Procedia Eng.* **2015**, *102*, 1918–1925. [[CrossRef](#)]
6. Chung, H.; Das, S. Processing and properties of glass bead particulate-filled functionally graded Nylon-11 composites produced by selective laser sintering. *Mater. Sci. Eng. A* **2006**, *437*, 226–234. [[CrossRef](#)]
7. Denchev, Z.; Dencheva, N. Polyamide Microcapsules and Method to Produce the Same. Patent No. PT PT10767914A, 6 March 2014.
8. Dencheva, N.; Denchev, Z.; Lanceros-Méndez, S.; Ezquerro Sanz, T. One-step in situ synthesis of polyamide microcapsules with inorganic payload and their transformation into responsive thermoplastic composite materials. *Macromol. Mater. Eng.* **2016**, *301*, 119–124. [[CrossRef](#)]
9. Sankaran, S.; Deshmukh, K.; Ahamed, M.B.; Pasha, S.K.K. Recent advances in electromagnetic interference shielding properties of metal and carbon filler reinforced flexible polymer composites: A review. *Compos. Part A Appl. Sci. Manuf.* **2018**, *114*, 49–71. [[CrossRef](#)]
10. Hu, M.; Gao, J.; Dong, Y.; Li, K.; Shan, G.; Yang, S.; Li, R.K.-Y. Flexible Transparent PES/Silver Nanowires/PET Sandwich-Structured Film for High-Efficiency Electromagnetic Interference Shielding. *Langmuir* **2012**, *28*, 7101–7106. [[CrossRef](#)]
11. Cano-Raya, C.; Dencheva, N.V.; Braz, J.F.; Malfois, M.; Denchev, Z.Z. Optical biosensor for catechol determination based on laccase-immobilized anionic polyamide 6 microparticles. *J. Appl. Polym. Sci.* **2020**, *137*, 49131. [[CrossRef](#)]
12. Dencheva, N.; Oliveira, S.; Braz, J.; Getya, D.; Malfois, M.; Denchev, Z.; Gitsov, I. Magnetically Responsive PA6 Microparticles with Immobilized Laccase Show High Catalytic Efficiency in the Enzymatic Treatment of Catechol. *Catalysts* **2021**, *11*, 239. [[CrossRef](#)]
13. Dencheva, N.V.; Vale, D.M.; Denchev, Z.Z. Dually reinforced all-polyamide laminate composites via microencapsulation strategy. *Polym. Eng. Sci.* **2016**, *57*, 806–820. [[CrossRef](#)]
14. Kurosu, H.; Ando, S.; Yoshimizu, H.; Ando, I. NMR Studies of Higher-order Structures of Solid Polymers. In *Annual Reports on NMR Spectroscopy*; Ando, I., Webb, G.A., Eds.; Academic Press: Cambridge, MA, USA, 1994; Volume 28, pp. 189–275.
15. Weeding, T.L.; Veeman, W.S.; Gaur, H.A.; Huysmans, W.G.B. Structural investigation of polyamide-6 and polyamide-6 composites using carbon-13 cross polarization/magic angle spinning NMR. *Macromolecules* **1988**, *21*, 2028–2032. [[CrossRef](#)]
16. Kubo, K.; Yamanobe, T.; Komoto, T.; Ando, I.; Shiibashi, T. Nylon 6 structure in solid state as studied by high-resolution ¹³C-NMR spectroscopy. *J. Polym. Sci. Part B Polym. Phys.* **1989**, *27*, 929–937. [[CrossRef](#)]
17. Kubo, K.; Ando, I.; Shiibashi, T.; Yamanobe, T.; Komoto, T. Conformations and ¹³C NMR chemical shifts of some polyamides in the solid state as studied by high-resolution ¹³C NMR spectroscopy. *J. Polym. Sci. Part B Polym. Phys.* **1991**, *29*, 57–66. [[CrossRef](#)]
18. Hatfield, G.R.; Glans, J.H.; Hammond, W.B. Characterization of structure and morphology in nylon 6 by solid-state carbon-13 and nitrogen-15 NMR. *Macromolecules* **1990**, *23*, 1654–1658. [[CrossRef](#)]
19. Mathias, L.J.; Powell, D.G.; Autran, J.-P.; Porter, R.S. Solid state ¹⁵N nuclear magnetic resonance of ¹⁵N-labeled nylon 6 and nylon 11: Observation of multiple crystalline forms and amorphous regions. *Mater. Sci. Eng. A* **1990**, *126*, 253–263. [[CrossRef](#)]
20. Powell, D.G.; Mathias, L.J. Characterization of nylon 6 by nitrogen-15 solid-state nuclear magnetic resonance. *J. Am. Chem. Soc.* **1990**, *112*, 669–675. [[CrossRef](#)]
21. Powell, D.G.; Mathias, L.J. Nitrogen-15 T1 measurements of semicrystalline nylon 6. *Macromolecules* **1989**, *22*, 3812–3814. [[CrossRef](#)]
22. Dencheva, N.; Nunes, T.; Oliveira, M.J.; Denchev, Z. Microfibrillar composites based on polyamide/polyethylene blends. 1. Structure investigations in oriented and isotropic polyamide 6. *Polymer* **2005**, *46*, 887–901. [[CrossRef](#)]
23. Dencheva, N.; Nunes, T.G.; Oliveira, M.J.; Denchev, Z. Crystalline structure of polyamide 12 as revealed by solid-state ¹³C NMR and synchrotron WAXS and SAXS. *J. Polym. Sci. Part B Polym. Phys.* **2007**, *43*, 3720–3733. [[CrossRef](#)]
24. Davis, R.D.; Jarrett, W.L.; Mathias, L.J. Solution and Solid-State NMR Spectroscopy of Nylon 6-Montmorillonite Clay Nanocomposites. In *Polymer Nanocomposites*; American Chemical Society: Washington, DC, USA, 2001; Volume 804, pp. 117–126.
25. Umek, P.; Huskić, M.; Škapin, A.S.; Florjančič, U.; Zupančič, B.; Emri, I.; Arčon, D. Structural and mechanical properties of polystyrene nanocomposites with 1D titanate nanostructures prepared by an extrusion process. *Polym. Compos.* **2009**, *30*, 1318–1325. [[CrossRef](#)]
26. Jouni, M.; Buzlukov, A.; Bardet, M.; Boisson, F.; Eddarir, A.; Massardier, V.; Boiteux, G. Skin effect of conductive polymer composites observed by high-resolution solid-state NMR. *Compos. Sci. Technol.* **2014**, *104*, 104–110. [[CrossRef](#)]
27. Brêda, C.; Dencheva, N.; Lanceros-Mendez, S.; Denchev, Z. Preparation and properties of metal-containing polyamide hybrid composites via reactive microencapsulation. *J. Mater. Sci.* **2016**, *51*, 10534–10554. [[CrossRef](#)]
28. Axelson, D.E.; Russell, K.E. Characterization of polymers by means of ¹³C NMR spectroscopy: (a) Morphology by Solid-State NMR (b) End-Group Studies. *Prog. Polym. Sci.* **1985**, *11*, 221–282. [[CrossRef](#)]
29. Bovey, F.A.; Jelinski, L.W. The observation of chain motion in macromolecules by carbon-13 and deuterium nuclear magnetic resonance spectroscopy. *J. Phys. Chem.* **1985**, *89*, 571–583. [[CrossRef](#)]
30. Torchia, D.A. The measurement of proton-enhanced carbon-13 T1 values by a method which suppresses artifacts. *J. Magn. Reson.* **1978**, *30*, 613–616. [[CrossRef](#)]
31. Campoy, I.; Gómez, M.A.; Marco, C. Structure and thermal properties of blends of nylon 6 and a liquid crystal copolyester. *Polymer* **1998**, *39*, 6279–6288. [[CrossRef](#)]

32. Ashiotis, G.; Deschildre, A.; Nawaz, Z.; Wright, J.P.; Karkoulis, D.; Picca, F.E.; Kieffer, J. The fast azimuthal integration Python library: *pyFAI*. *J. Appl. Crystallogr.* **2015**, *48*, 510–519. [[CrossRef](#)]
33. Vasiliu-Oprea, C.; Dan, F. On the relation between synthesis parameters and morphology of anionic polycaprolactone obtained in organic media. I. Influence of the Na[O(CH₂)₂OCH₃]₂AlH₂/isophorone diisocyanate catalytic system. *J. Appl. Polym. Sci.* **1996**, *62*, 1517–1527. [[CrossRef](#)]
34. Zoya, B. Popović, B.D.P. The skin effect. In *Introductory Electromagnetics*; Prentice-Hall Inc.: Hoboken, NJ, USA, 1999; pp. 382–392.
35. Oliveira, F.M. Development and Optimization of a Novel Microcapsule Polyamide Platform and Its Application for the Fabrication of High-Performance Magnetic, Electro-Shielding and High k Thermoplastic Composites. Ph.D. Thesis, University of Minho, Guimarães, Portugal, 2020.
36. Schreiber, R.; Veeman, W.S.; Gabriëls, W.; Arnauts, J. NMR Investigations of Orientational and Structural Changes in Polyamide-6 Yarns by Drawing. *Macromolecules* **1999**, *32*, 4647–4657. [[CrossRef](#)]
37. Bovey, F.A.; Mirau, P.A. The dynamics of macromolecules. In *NMR of Polymers*; Bovey, F.A., Mirau, P.A., Eds.; Academic Press: San Diego, CA, USA, 1996; pp. 353–453. ISBN 978-0-12-119765-0.
38. Jelinski, L.W.; Melchior, M.T. High-Resolution NMR of Solids. *Appl. Spectrosc. Rev.* **2004**, *35*, 25–93. [[CrossRef](#)]